Journal of Naval Architecture and Marine Engineering
January, 2026
https://dx.doi.org/10.3329/jname.v23i1.77931 *http://www.banglajol.info*

EFFECT ON THE PERFORMANCE OF B-SERIES PROPELLERS WITH VARIATION IN INSTALLATION ANGLE OF PROPELLER BOSS CAP FIN

M. Yamin[1], R. Irawan[1*], C. P. Mahandari[1], F. K. Anwar[2], and R. Firmansyah[2]
[1]Mechanical Engineering Department, Gunadarma University, Jl. Margonda Raya 100 Depok, West-Java, Indonesia, mohay@staff.gunadarma.ac.id ; rirawan2010@gmail.com* ; coki@staff.gunadarma.ac.id
[2]Center for Automotive Research, Gunadarma University, Jl. Margonda Raya 100 Depok, West-Java, Indonesia, fikrikhairulanwar17@gmail.com ; rfrmnsyh10@gmail.com

Abstract:

This study examines the influence of Propeller Boss Cap Fins (PBCFs) on the hydrodynamic performance of B-series propellers by introducing variations in installation angles. While PBCFs are widely recognized for their potential to reduce rotational losses and enhance propulsion efficiency, the specific impact of installation angle variation—particularly in the context of electric-powered vessels—has remained underexplored. To address this gap, the present work focuses on the aerodynamic optimization of PBCFs, varying the installation angle between −5° and 5°, using a NACA4412 airfoil profile within a Computational Fluid Dynamics (CFD) framework. The analysis is conducted using the Reynolds-Averaged Navier-Stokes (RANS) approach with a Grid Independence Test (GIT) performed to ensure numerical accuracy. Validation of the simulation results against available experimental data confirms the reliability of the model. The configuration featuring a 2° PBCF installation angle demonstrates the most favorable performance, yielding an increase in the thrust coefficient (K_T) from 0.3719 to 0.3797 and an improvement in open water efficiency (η) by 4.3% relative to the baseline CFD model. Additionally, a maximum efficiency enhancement of 24% is observed when compared to experimental data at an advance coefficient of J = 0.415. The validation results exhibit a maximum deviation of 9.934% at lower rotational speeds, which is within an acceptable range for engineering applications, particularly given the challenges of modeling complex flow phenomena at low Reynolds numbers. The principal contribution of this study lies in its systematic evaluation of PBCF installation angle as a design variable—an area that has received limited attention in existing literature. The findings demonstrate that even minor angular modifications can significantly influence propeller performance. More broadly, this research contributes to the advancement of energy-efficient marine propulsion technologies by offering a validated, CFD-based design methodology. The implications are particularly relevant for the development of sustainable propulsion systems in electric and low-emission vessels, supporting broader efforts to reduce fuel consumption and minimize environmental impact in maritime operations.

Keywords: B-series propellers, propeller boss cap fins (PBCFs), CFD simulation, installation angle optimization, propeller efficiency, electric propulsion, hydrodynamic optimization, maritime sustainability.

NOMENCLATURE

$\bar{u}, \bar{v}$	velocity components
u, v	dimensionless velocity components
K_T	thrust coefficient
K_Q	torque coefficient
T	trust
J	advance ratio
D	propeller diameter
V_A	speed of advance
n	propeller revolution rate

Greek symbols

β	coefficient of thermal expansion
ν	kinematic viscosity
η	open water efficiency
ρ	water density
Q	torque
ω	angular velocity
k	turbulent kinetic energy
p	pressure
ε	turbulent dissipation

 Received on: Nov., 2024

1. Introduction

In the last few years, energy saving and emission reduction have become very important issues in the maritime industry. As an archipelagic country, maritime transportation in Indonesia plays a key role in the economy and the distribution of goods. Hence, improving energy efficiency and reducing greenhouse gas emissions on ships become increasingly crucial. As the demand on maritime transportation increases, it is estimated that the shipping sector may contribute up to 17% of total global carbon dioxide emissions by 2050 if there is no appropriate intervention (Kim *et al.*, 2021).

To address the issue of carbon emission, the International Maritime Organization (IMO) has implemented the Energy Efficiency Design Index (EEDI) standard. The standard regulates carbon dioxide emissions of a ship, which is based on its design (Hasan and Karim, 2023). This standard requires new ships to meet certain emission limits. The ships that do not meet the EEDI standard are not allowed to be built. It encourages the ship designers or developers conduct further researches to reduce this EEDI value (Lee, 2024). The method that has proven effective is the method using Energy Saving Devices (ESD) (Adietya *et al.*, 2023), such as Propeller Boss Cap Fins (PBCF). PBCF was first developed in 1987 and since then, it has been shown to improve propeller efficiency by reducing vortices around the rear of the propeller, resulting in increased thrust efficiency (Ismail *et al.*, 2024). PBCF consists of small fins mounted around the propeller hub cover and has a minimal angle of attack (Martinelli *et al.*, 2021). These devices can be installed in various areas, such as in front of the propeller (Region I) to reduce drag or create favourable wake, in the propeller area (Region II) to reduce torque or increase thrust, and in the rudder area (Region III) for similar purposes.

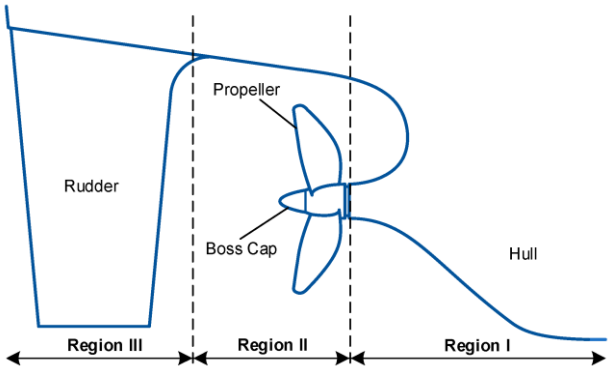

Fig. 1: Classification of the regions for aft ship energy saving devices (Yin *et al.*, 2023)

In addition to energy efficiency, cavitation is one of the critical problems that can significantly reduce propeller performance and lifespan. Cavitation is a phenomenon where vapor bubbles form in low-pressure regions on the propeller surface and collapse violently, leading to vibration, noise, thrust loss, and erosion damage to the propeller material. Erosion due to cavitation not only reduces efficiency but can also compromise the structural integrity of the propeller over time (Mohammadizadeh *et al.*, 2024; Wang *et al.*, 2025). A recent study by (Zhang *et al.*, 2025) emphasized the importance of mitigating cavitation in multiphase flows to enhance the durability and operational safety of propulsion systems.

The application of PBCF is not only beneficial for increasing efficiency but also for mitigating cavitation effects. By suppressing the hub vortex and improving wake flow uniformity, PBCF reduces the intensity of low-pressure zones and turbulent vortices that often trigger cavitation near the propeller boss and blade root. This effect contributes to a smoother flow field, reducing the cavitation-induced erosion risk and prolonging propeller service life. Therefore, integrating PBCF offers dual benefits—energy efficiency enhancement and cavitation damage reduction—which makes it a highly relevant solution in sustainable ship propulsion design. Researches show that the integration of PBCF with various types of propellers, such as B4-70 and Ka4-70, can significantly improve the efficiency of propeller. For an example, the B4-70 propeller with PBCF showed an efficiency increase of between 3% and 5% when the advance ratio (J) varied from 0 to 0.7, while the Ka4-70 recorded an increase of 1% to 3% under similar conditions (Adietya *et al.*, 2024). In addition, the use of PBCF on the E698 model propeller with a configuration such as P45-R90 was able to improve pressure distribution and reduce vortex formation. However, these results depended on the configuration used (Göksu *et al.*, 2024).

Recent advancements in computational methods, such as Fluid-Structure Interaction (FSI) and machine learning algorithms, have enabled more precise optimization of PBCF designs. For example, a study coupling BP neural networks with optimization algorithms achieved a 12% efficiency gain in propeller performance (Li *et al.*, 2024). Additionally, investigations into porous media effects on fluid dynamics have provided insights into drag reduction techniques applicable to marine propellers (Mohammadizadeh *et al.*, 2021).

Sustainability-focused research has also highlighted the role of PBCFs in reducing greenhouse gas emissions, aligning with global decarbonization goals (Vásconez Garcia *et al.*, 2024). Furthermore, studies on sediment transport and cavitation effects (Gavidia *et al.*, 2024; Gavidia *et al.*, 2023) have informed the design of more durable and efficient propeller systems.

Further research on propellers combined with PBCF showed that the Ka4-70 propeller with the 19A divergent Nozzle and PBCF could achieve a 12% efficiency improvement at high forward ratios (J = 0.7 to 1.0) (Adietya *et al.*, 2024). In addition, the B4-70 propeller with a convergent boss cap shape and a 15-degree inclination showed a 3% to 8% efficiency improvement at higher forward ratios (J = 0.8 to 1.0) (Adietya *et al.*, 2023). Optimization of the PBCF design, including the use of airfoil shapes, has also been explored. It showed that the best performing profiles can produce significant efficiency gains by suppressing hub vortices and providing extra thrust, which makes them feasible for industrial applications (Yin *et al.*, 2023). Overall, the integration of PBCF into propeller design is promising to improve the efficiency of marine vessels, which can contribute to sustainable maritime operations.

The application of PBCF on propellers contributes to various innovative designs to optimize efficiency. The research on the installation angle of PBCF reveals that variations in the installation angle can significantly affect the flow and pressure distribution, which can contribute to improve the overall efficiency of the propeller/rudder system. This study leads to the optimal PBCF design for a four-blade B-series propeller with a diameter of 600 mm, an expanded area ratio (Ae/Ao) of 0.65, and a pitch-to-diameter ratio (P/D) of 1.10627 with a rake of 15°. This propeller uses Ni-Al Bronze material, providing robust and efficient performance (Barnitsas *et al.*, 1981; Lovibond *et al.*, 2023).

The significant contribution of this study lies in the variation of the installation angle (α) in the range of $-5° \leq \alpha - \varepsilon \leq 5°$ with the application of the NACA4412 airfoil design and the divergent boss cap type. This approach is different from the previous studies that focused on the convergent type (Yin *et al.*, 2023). It provides an important contribution to the understanding of aerodynamic performance that has not been explored in depth before. This study aims to systematically identify the most effective profiles and angles in improving energy efficiency. Through comprehensive CFD simulations in this study, the optimal PBCF design not only shows significant energy efficiency improvements but also proves to be feasible for application in the maritime industry. It is expected that this innovation can be a new design solution that can improve propeller performance and reduce energy consumption in the shipping industry.

This study aims to systematically identify the most effective PBCF profiles and installation angles in enhancing energy efficiency using a B-series four-blade propeller. The optimal design is evaluated through CFD simulation with a RANS approach and validated against experimental data. The structure of this paper is organized as follows: Section 1 introduces the background, problem, and objectives. Section 2 explains the numerical method, including the geometry, meshing, boundary conditions, turbulence model, and validation. Section 3 presents the results and discussion of the simulation, focusing on thrust coefficient, efficiency, and flow characteristics for different installation angles. Finally, Section 4 concludes the study and discusses its practical implications for ship propulsion optimization.

2. Numerical Methods

2.1 Governing equations

Computational Fluid Dynamics (CFD) is a necessary in modern engineering that uses numerical analysis to simulate and analyze fluid flow (Li *et al.*, 2024). CFD is employed in various applications, such as optimizing propeller designs and analyzing the relationship between flow speed, torque, and power to achieve optimal thrust

(Lovibond *et al.*, 2023; Pantel *et al.*, 2024). The methodology of CFD relies on fundamental fluid flow equations, specifically the following Navier-Stokes equations for incompressible viscous fluids (Rastogi and Mathew, 2022):

$$\frac{\delta u_i}{\delta t} + \frac{\delta}{\delta x_j}\left(u_i u_j\right) = \frac{\delta p}{\delta x_i} + v\frac{\delta^2 u_i}{\delta x_j \delta x_j} \quad (1)$$

$$\frac{\delta u_i}{\delta x_j} = 0 \quad (2)$$

where u represents fluid velocity, p is pressure, ρ is density, and v is kinematic viscosity.

These equations allow for the prediction of thrust and torque in propeller analysis.

The standard κ-ϵ turbulence model is used in CFD to describe turbulent flow. This model is based on transport equations for turbulent kinetic energy (κ) and dissipation rate (ϵ) (Hunt, 1973). However, the assumption that the flow is fully turbulent limits the model's applicability to highly turbulent flows (Launder, 1995).

CFD facilitates propeller design optimization by analyzing hydrodynamic characteristics and validating models against experimental data, resulting in more efficient and environmentally friendly maritime applications. In open water, propeller characteristics are typically represented by thrust and torque coefficients, as well as the advance coefficient J, which are defined as follows (Fitriadhy *et al.*, 2023):

$$J = \frac{V_a}{nD} \quad (3)$$

where V_a is the advance speed, n is the rotational speed in revolutions per second, and D is the propeller diameter. Advance Coefficient (J): This coefficient is a dimensionless parameter that relates the forward velocity of the vessel to the propeller's rotational speed and diameter.

Thrust Coefficient (K_T): This coefficient represents the thrust produced by the propeller relative to the fluid density, rotational speed, and diameter.

$$K_T = \frac{T}{\rho n^2 D^4} \quad (4)$$

where T is the thrust, ρ is the fluid density, n is the propeller's rotational speed, and D is the propeller diameter.

Torque Coefficient (K_Q): This coefficient indicates the torque produced by the propeller, normalized by the same parameters as the thrust coefficient.

$$K_Q = \frac{Q}{\rho n^2 D^5} \quad (5)$$

where Q is the torque.

Efficiency (η): The propeller's efficiency in open water is calculated using the advance coefficient, the thrust and torque coefficients.

$$\eta = \frac{J}{2\pi}\frac{K_T}{K_Q} \quad (6)$$

The advance coefficient J is used to convert the vessel's speed V_s, which is equal to the advance speed V_a (assuming no wake effects in open water analysis), into a dimensionless form using the propeller's tip speed.

Thrust T and torque Q are also normalized to be dimensionless by using the propeller's rotational speed n, diameter D, and fluid density ρ.

The open water propeller curves are constructed such that K_T, K_Q, and n are functions of J. Typically, K_Q is multiplied by ten for better presentation on a single set of axes.

The percentage difference between experimental results and CFD simulations is calculated to evaluate the accuracy of the CFD model. This is calculated using the following equations:

$$\Delta K_T(\%) = \frac{K_{TCFD} - \Delta K_{TEXP}}{\Delta K_{TEXP}} \quad (7)$$

where $K_{T,CFD}$ is the thrust coefficient from CFD results and $K_{T,EXP}$ is the experimental thrust coefficient.

$$\Delta K_Q(\%) = \frac{K_{QCFD} - \Delta K_{QEXP}}{\Delta K_{QEXP}} \quad (8)$$

where $K_{Q,CFD}$ is the thrust coefficient from CFD results and $K_{Q,EXP}$ is the experimental thrust coefficient.

$$\Delta \eta(\%) = \frac{\eta_{CFD} - \eta_{EXP}}{\eta_{EXP}} \quad (9)$$

where η_{CFD} is the efficiency from CFD results and η_{EXP} is the experimental efficiency. These calculations help in assessing the performance and accuracy of the CFD simulations in predicting the propeller's performance compared to experimental data.

2.2 Solver and boundary conditions

The ANSYS software simulation is based on the finite volume method. In this study, pressure-based simulations were performed as the primary parameter, and simulations were conducted in both steady and unsteady states as shown in Table 1. The simulations were performed using the RANS (Reynolds Averaged Navier-Stokes) method, integrated with the blade element theory (BET) in Ansys Fluent 2023 R1 (Pantel *et al.*, 2024), to accurately predict the propeller thrust and drag. The Multi Reference Frame (MRF) model was used to model the propeller rotation, as shown in Table 2, and the k-ω SST (Shear Stress Transport) turbulence model was selected because of its effective ability to capture phenomena such as flow separation and cavitation effects (Zhang *et al.*, 2023). Several assumptions were applied to simplify the simulation of the propeller hydrodynamic characteristics, including the assumption of steady flow, non-cavitation, and incompressible flow, so that a single-phase model was used. The fluid used was fresh water with a density of ρ = 1000 kg/m³ and a viscosity of 0.001003 kg/(m s). The conditions of the cell zone and boundaries are described in Table 3. to match the simulation conditions with the propeller application in this study. Electric-powered ships in freshwater environments such as rivers and lakes were used. The rotation of the propeller corresponds to the rotation of the rotor domain, meaning that the rotation of the propeller depends on the rotating domain with the conditions that match the configuration of the cell zone.

Table 1: Simulation flow conditions

Case Number	Rotational Speed n (rps)	Velocity of Advance (U) m/s	Advanced Coefficient (J)
1	30	6.22	0.346
2	25	6.22	0.415
3	20	6.22	0.518
4	17.5	6.22	0.592
5	15	6.22	0.691

The Second-Order Upwind setting was used to achieve accurate results and more efficient computation. It improves accuracy at the cost of higher computational time as recommended by previous studies (Lovibond *et al.*, 2023; Rastogi and Mathew, 2022). The details of the solver settings are presented in Table 4. In the simulation, the numerical algorithm used the coupled method as it offers faster convergence, higher accuracy, better stability, and flexibility for different types of flows compared to the SIMPLE method (Chandukrishna and Venkatesh, 2023). This study was chosen as a steady-state simulation where the momentum equation was solved to obtain

the velocity field, while the pressure gradient was determined based on the initial conditions or previous iterations considering the pressure distribution. The solution gradient was calculated using the Least-Squares Cell-Based approach as it offers comparable accuracy with lower computational requirements. Since the simulation domain included a large number of cells, considering the large number of cells in the simulation domain, the Second-Order Upwind was chosen to address the need for high accuracy in efficient computational time.

Table 2: Cell zone conditions

Condition	Value
Motion Frame	Rotating Domain Relative to cell zone Absolute
Rotation-axis origin (X, Y, Z)	(0,0,0)
Rotation axis direction (X, Y, Z)	(0,0,1)
Rotational velocity	Diff. velocity corresponding with n
Stationary domain Motion	Stationary

Table 3: Boundary conditions

Condition	Value
Time	Transient
Turbulent Model	Kw-SST
Density	1000 kg/m^3
Viscosity	1.7894 x 10^{-5} kg/ms
Velocity magnitude	6.22 m/s
Coordinate system (X, Y, Z)	(0,0,1)
Turbulent intensity	5%
Pressure outlet Backflow reference frame	Absolute
Backflow direction	Normal to boundary
Turbulent intensity	5%
Outer enclosure wall Wall motion	Stationary
Wall condition	No slip
Propeller blade Wall motion	Stationary
Wall condition	No slip

Table 4: Solver setting

Parameter	Setting
Pressure Link	Coupled
Pressure	Standard
Velocity Formulation	Absolute
Gradient	Least Squares Cell Based
Momentum	Second Order Upwind
Turbulent Kinetic Energy	Second Order Upwind
Turbulent Dissipation Rate	Second Order Upwind
Turbulence Model	Standard kw-SST
Near Wall Treatment	Standard Wall Functions
Models	Single Phase
Solver	Steady

2.3 Geometry modeling and modification

In this study, the baseline model of the Wageningen B-Series propeller was adopted from the experiments conducted by Barnitsas *et al.* (1981) and the CFD studies conducted by Lovibond *et al.* (2023); Tarafder *et al.* (2023). Figure 2 shows (a) Front view of the propeller, (b) Side view of the propeller and (c) Side view of the boss cap, where Dp represents the propeller diameter, and Dbc, rbc, lbc, and φ denote the diameter, radius, length, and angle of the boss cap, respectively, with φ<0, indicating a divergent boss cap. The Design of Experiments (DOE) method was applied to optimize the shape and performance of the propeller. This approach allows

researchers to systematically control design variables, such as the number of blades, rake angle, and water speed, to understand their impact on aerodynamic performance and energy efficiency as shown in Table 5.

The propeller geometry in this study was created using tools provided in the Wageningen site to generate a 3D model of the B-Series propeller. This propeller model was then imported into CAD software for modification using SolidWorks 2020 as shown in the following figures. The boss cap covers the hub area of the propeller and is used to enhance the hydrodynamic performance of the propeller and ship handling. In this study, the B-Series propeller was modified by adding divergent boss caps. The geometric design of the modified boss cap is shown in the following Figure 3. In addition, the fins on the boss cap were modified with varying installation angles ranging from $-5° \leq \alpha - \varepsilon \leq 5°$. The parameters of propeller are detailed in Table 6.

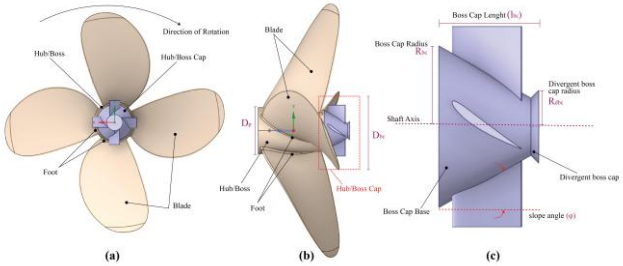

Fig. 2: Propeller and boss cap: (a) front view of the propeller, (b) side view of the propeller and (c) side view of the boss cap, and angle $\varphi<0$ for a divergent design

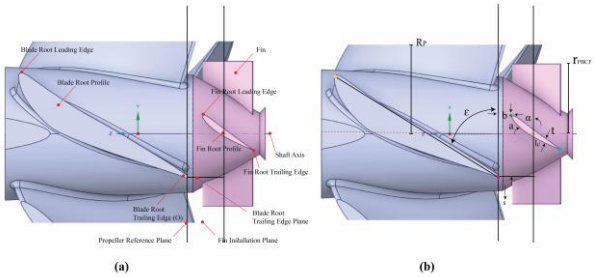

Fig. 3: Modification of propeller and optimization of boss cap design

Table 5: Propeller geometry specifications

Specification	Details
Propeller Type	B-series
Rotation Direction	Clockwise
Blade Diameter (d)	600 mm
Number of Blades (z)	4 blades
Expanded Area Ratio (Ae/Ao)	0.65
Hub Length	155.56 mm
Pitch-to-Diameter (P/D) Ratio	1.10627
Rake	15°
Material	Ni-Al Bronze
Engine Rotation Speed	3500 RPM
Gear Ratio	3:1
Propeller Rotation	Variable

Table 6: Boss cap specifications

Parameter	Cap Divergent
Type	Divergent
Length	0.1Dprop
D1	Dhub
D2	0.45Dhub
Slope	29,5°

Table 7: PBCF Foil Design Parameters

Parameter	PBCF Foil
Shapes	NACA 4421
Number of fins/foils	4
Chord Length, lc	50 mm
Max Thickness, t	0.114c
DPBCF	0.2Dprop
Installation Angle, α	$-5° \leq \alpha - \varepsilon \leq 5°$
Phase lag angle (º)	0
RakePBCF	0

2.4 Computational domain

The simulation domain is divided into three parts: Fixed domain, rotating domain, and propeller. Fixed domain and rotating domain serve as fluid flow domains, while the propeller is considered as a wall. Fixed domain is static and is the path of water flow, while rotating domain, where the propeller rotates, is the main focus for calculating propeller performance, both baseline and modified. FLUENT provides various boundary conditions such as pressure inlet, velocity inlet, mass flow inlet, pressure outlet, pressure far-field, outlet flow, stationary wall, moving wall, and axis. These boundary conditions are set to define the system by setting the geometry as needed. For example, setting the inlet on a certain side as the inlet, defining the outlet on the outflow side, or defining the interface as the boundary between the rotating zone and the still zone as are described in Figure 4.

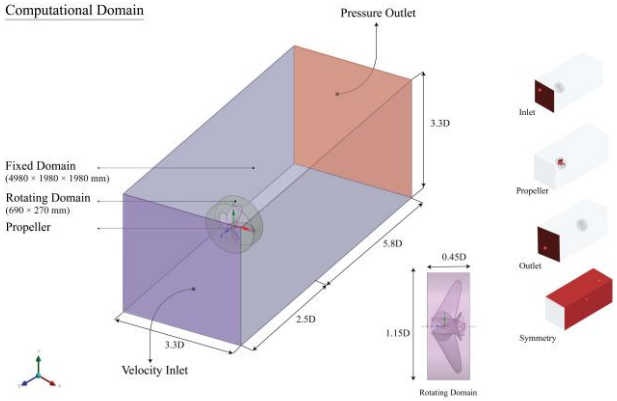

Fig. 4: Computational domain

2.5 Meshing set-up

Meshing is the process of discretizing a continuous fluid domain becoming a discrete computational domain, so that it can be solved and yield a solution. The mesh is generated using the meshing tool in Ansys Fluent, which produces an unstructured tetrahedral grid discretization crossing all static (tunnel) and rotating (rotor) domains. This type of mesh can effectively discretize complex geometries with or without user intervention and configuration. In this study, the meshing was applied to the fixed domain, rotor, and propeller, as shown in Figure 5.

Tables 8 - 10 provide details about the mesh options, positioning settings, and mesh quality used in the CFD simulation for modeling the propeller and fin blades. Table 8 describes the element size settings for various parts of the simulation domain, such as the propeller blades, fin blades, rotating domains and stationary domains. Face sizing was applied to the propeller blades, fin blades, and rotating domains with element sizes of 8 mm, 5 mm, and 15 mm, respectively. Meanwhile, body sizing for the rotating and stationary domains was set with an element size of 50 mm.

Table 9 outlines the global meshing details, including the general parameters used for the entire domain. These parameters cover CFD physical preferences, solver preferences for Fluent, and linear element ordering. The default element size is 100 mm, with a maximum adaptive size of 200 mm, a mesh growth rate of 1.2, and a mesh size for capturing small features of 0.5 mm. Other settings include a minimum curvature size of 1 mm and a normal curvature angle of 18°. Table 10 provides information about mesh quality, specifically for CFD physics. Physical and solver preferences remain set for CFD and Fluent, with linear element ordering and a default element size of 100 mm. The maximum adaptive size remains 200 mm, indicating consistency in applying mesh settings to ensure accurate and efficient simulations. This meshing configuration was applied to all simulated models, ensuring uniform mesh size and quantity across different models, allowing for accurate comparative studies.

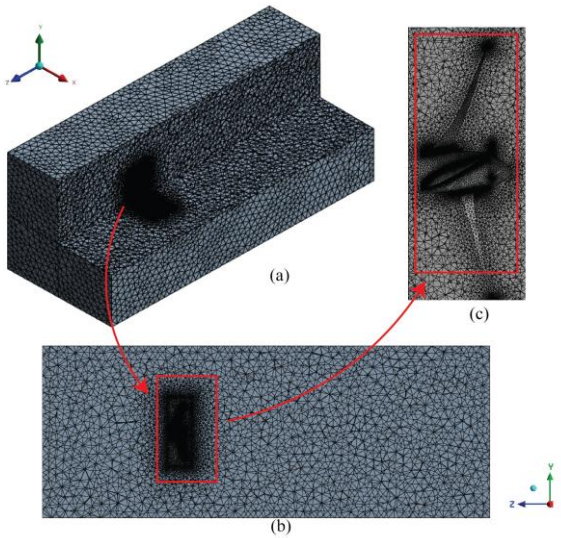

Fig. 5: Meshing setup for the propeller simulation: (a) fixed domain, (b) rotating domain, and (c) propeller.

Table 8: Mesh Options and Positioning

Mesh Options	Position	Element Size (mm)
Face sizing	Propeller blade	8
	Fin blade	5
	Rotating domain	15
Body sizing	Rotating domain	50
Body sizing	Stationary domain	50

Table 9: Global Meshing Details

Parameter	Value
Physics preference	CFD
Solver preference	Fluent
Element order	Linear
Element size	Default (100 mm)
Max adaptive size	Default (200 mm)
Growth rate	Default (1.2)
Mesh defeaturing size	Default (0.5 mm)
Curvature min size	Default (1 mm)
Curvature normal angle	Default (18.0°)

Table 10: Mesh Quality

Parameter	**CFD Physics**
Physics preference	CFD
Solver preference	Fluent
Element order	Linear
Element size	Default (100 mm)
Max adaptive size	Default (200 mm)

3. Results and Discussion

3.1 Grid independence test

A Grid Independence Test (GIT) is a crucial procedure in CFD to ensure that the simulation results are not affected by the grid resolution or configuration, as illustrated in Figure 6. This test involves running simulations with varying grid resolutions to verify if the results converge to a certain value or not. This ensures that the grid used is sufficient to capture the important physical aspects of the problem being studied. However, since there are no standard guidelines for grid independence test, the researchers often rely on self-judgment, which can affect the subjectivity of the results Lee *et al.* (2020a); Lee *et al.* (2020b). The mesh sensitivity test also aims to ensure that the mesh used is suitable for simulation conditions, i.e., when convergence is achieved, and the most accurate K_T and K_Q results are obtained at the appropriate mesh size. Mesh stability can be assessed by the consistency of output parameter values from multiple simulations under different mesh conditions. If changes in mesh size do not significantly affect the output values, the simulation has reached an optimal mesh (grid size).

In this study, three types of meshes which were fine, medium, and coarse were simulated. The details of each mesh are shown in Table 11. The GIT was performed at 30 RPS with J = 0.346 at a speed of 6.22 m/s, with a turbulent intensity of 5% applied to all configurations. From the GIT results shown in Table 11, the medium mesh was finally chosen as the minimum mesh size to be applied to all VAWT configurations studied, as it resulted in a K_T error of 0.508% with a significantly shorter computation time.

Table 11: Grid independence test

Baseline GIT						**Error**	
Type	Element	T	K_T	Q	K_Q	K_T	K_Q
Coarse	1388769	43472.981	0.37338	4181.159	0.05985	0.914	-20.197
Medium	2483659	43297.858	0.37188	4185.445	0.05991	0.508	-20.115
Fine	3774442	43332.274	0.37217	4209.012	0.06025	0.588	-19.665

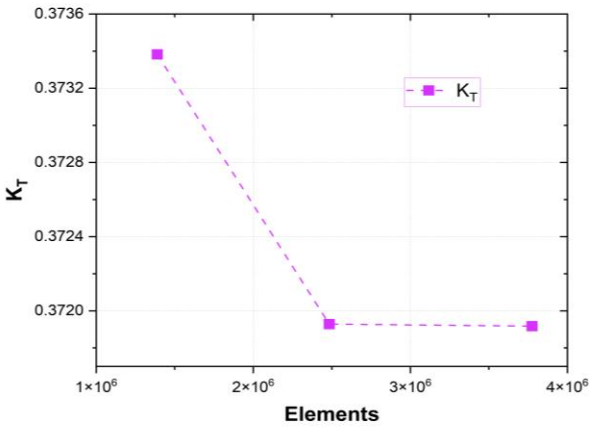

Fig. 6: Mesh convergence graph

3.2 Validation with experimental data and previous CFD simulations

The developed simulation model was validated by comparing the results of simulation with experimental data (Barnitsas *et al.*, 1981), where 120 B series propeller models were tested and analyzed by double polynomial regression in the Netherlands Ship Model Basin in Wageningen. The obtained double polynomials express the thrust coefficient, torque, and their relation to the number of blades, blade area ratio, pitch-diameter ratio, and advance coefficient, and previous CFD simulations conducted by Lovibond *et al.* (2023). The results indicate that at a rotational speed of 30 RPS, the simulated K_T value is 0.372, exhibiting a discrepancy of only 0.507% relative to the experimental data. It indicates that this simulation model is capable of replicating experimental results with good accuracy. However, compared to the CFD results by (Lovibond *et al.*, 2023), there was a difference of 6.800%, suggesting some differences in assumptions or methodologies used between the two simulations, as shown in Table 12. At lower rotation speeds, such as 25 RPS, the difference between simulation and experimental results increased to -7.073%, indicating that the simulation model tends to slightly underestimate the thrust coefficient under these conditions. Nevertheless, the comparison with CFD results showed a smaller error of 1.558%. It indicates that despite the differences from experimental data, the simulation results remain consistent with previous studies.

As the rotation speed further decreases, for example at 20 RPS, the error against experimental data becomes more significant, reaching -9.934%. However, these simulation results are almost identical to the CFD results, with only a 0.005% difference, indicating that the model is still highly accurate compared to the previous simulations. Even at lower speeds, such as 17.5 RPS and 15 RPS, the simulation model continues to show reasonably good consistency. The results show slight differences between the simulation and experimental results, with errors of -7.525% and -5.465%, respectively. Compared to the CFD results, the errors at these two speeds are also relatively small, at -1.042% and -2.289%, respectively, indicating that the model remains valid even under different operating conditions. Overall, the results show that the simulation model is quite accurate in predicting the thrust coefficient compared to experimental data and previous CFD results, even though there are some variations at different rotation speeds. The differences could be due to variations in boundary conditions, numerical methods, or assumptions used in the simulations. The results provide a strong basis for model validation but also indicate potential areas for further adjustment to enhance the accuracy, as shown in Table 12.

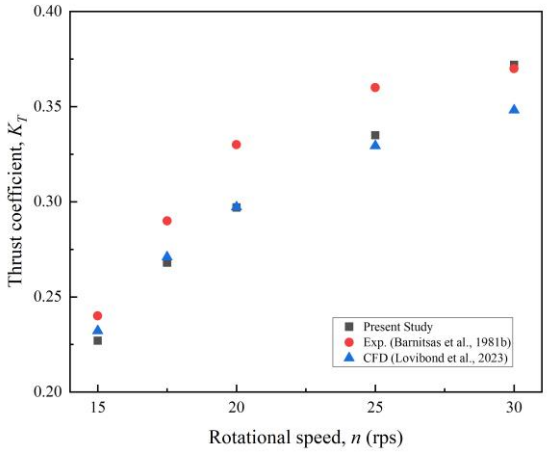

Fig. 7: Graph Validation Present Study with Experiment and Simulation

Table 12: Validation Model Baseline Comparing Experiment with Simulation Results

RPS	**Present Result**				**Exp. (Barnitsas *et al.*, 1981b)**		**CFD (Lovibond *et al.*, 2023))**	
	T	Q	K_T	K_Q	K_T	Error%	K_T	Error%
15	6603.999	708.20	0.227	0.041	0.240	-5.465	0.2322	-2.289
17.5	10624.74	1097.21	0.268	0.046	0.290	-7.525	0.271	-1.042

20	15380.01	1558.12	0.297	0.050	0.330	-9.934	0.2972	0.005
25	27048.51	2691.52	0.335	0.055	0.360	-7.073	0.3294	1.558
30	43297.86	4185.44	0.372	0.06	0.370	0.507	0.3482	6.800

3.3 Impact of PBCF modification on propeller performance

Figures 8 to 18 show the results of the propeller simulation with the modification of the installation angle on the PBCF. Overall, the use of PBCF can improve the efficiency of the propeller performance. Modification of the PBCF with an installation angle of 2 degrees results in significant changes in K_T and K_Q (Figure 10). At J=0.346, K_T increases from 0.3719 in the baseline configuration to 0.3797 with the modification, indicating an enhanced thrust-producing capability, as summarized in Table 13. In contrast, K_Q shows a slight reduction, decreasing from 0.0599 to 0.0594. It indicates that a reduction in the torque load is required to produce the same thrust. The propeller efficiency also improves consistently with the modification of the PBCF. For example, at J = 0.346, the propeller efficiency increases from 0.3417 (baseline) to 0.3517 (modification), indicating that the propeller with PBCF modification is more effective in converting energy into thrust. Moreover, this model modification increases efficiency about 4.3%, which is significantly higher than previous studies that only reached 1.043% Yin *et al.* (2023). Compared with the experimental results, this model achieves an efficiency of about 24% at J = 0.415. This efficiency improvement contributes to the overall better performance of the propeller.

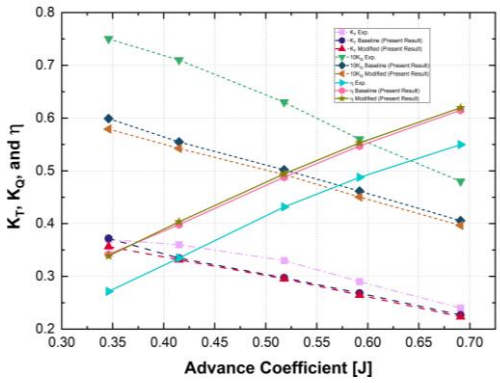

Fig. 8: Comparison Graph of K_T, K_Q, and η for Baseline PBCF and Modified PBCF with 0 Degree Installation Angle

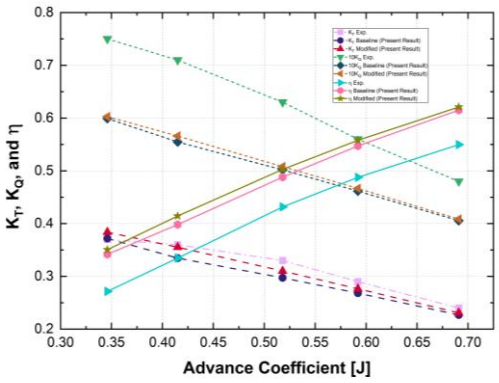

Fig. 9: Comparison Graph of K_T, K_Q, and η for Baseline PBCF and Modified PBCF with 1 Degree Installation Angle

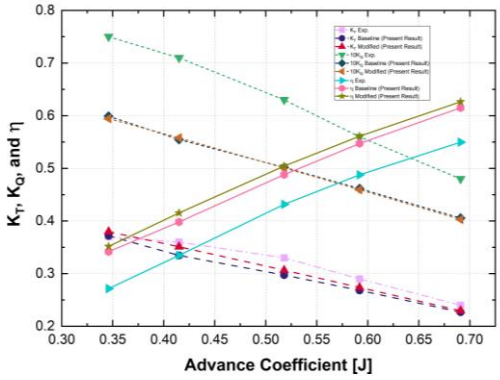

Fig. 10: Comparison Graph of K_T, K_Q, and η for Baseline PBCF and Modified PBCF with 2 Degree Installation Angle

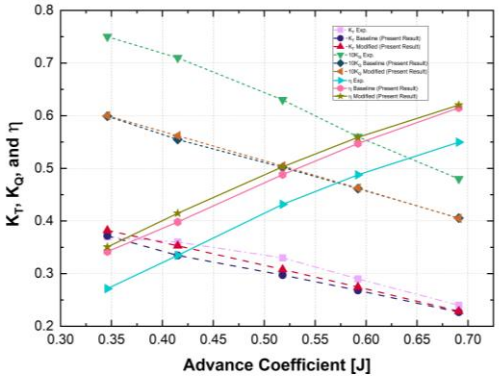

Fig. 11: Comparison Graph of K_T, K_Q, and η for Baseline PBCF and Modified PBCF with 3 Degree Installation Angle

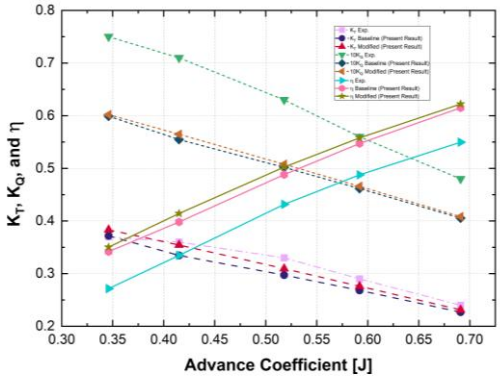

Fig.12: Comparison Graph of K_T, K_Q, and η for Baseline PBCF and Modified PBCF with 4 Degree Installation Angle

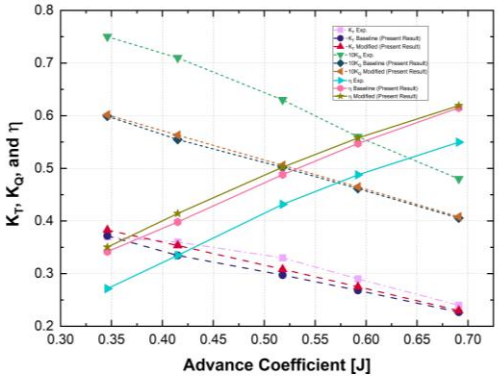

Fig. 13: Comparison Graph of K_T, K_Q, and η for Baseline PBCF and Modified PBCF with 5 Degree Installation Angle

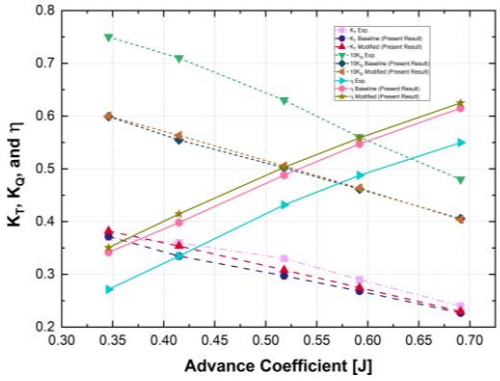

Fig. 14: Comparison Graph of K_T, K_Q, and η for Baseline PBCF and Modified PBCF with -1 Degree Installation Angle

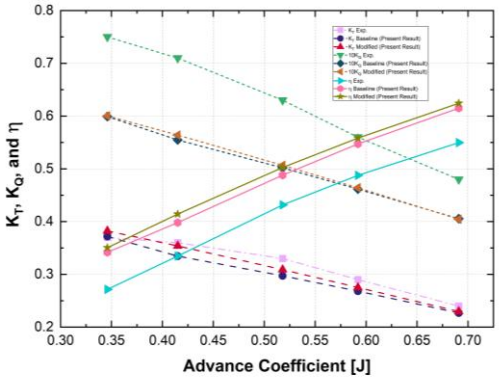

Fig. 15: Comparison Graph of K_T, K_Q, and η for Baseline PBCF and Modified PBCF with -2 Degree Installation Angle

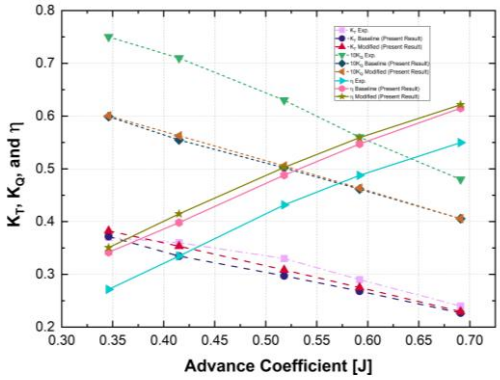

Fig.16: Comparison Graph of K_T, K_Q, and η for Baseline PBCF and Modified PBCF with -3 Degree Installation Angle

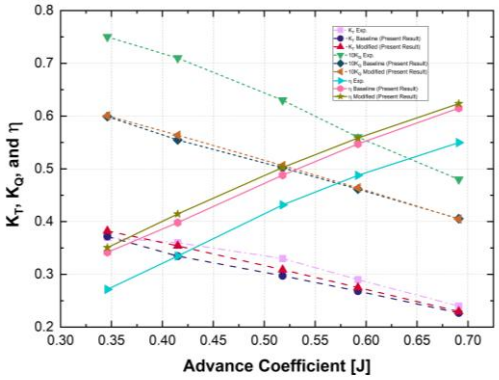

Fig. 17: Comparison Graph of K_T, K_Q, and η for Baseline PBCF and Modified PBCF with -4 Degree Installation Angle

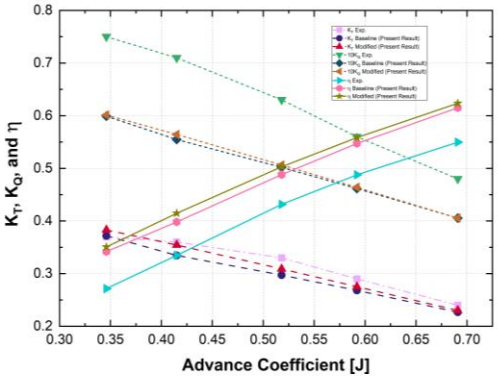

Fig. 18: Comparison Graph of K_T, K_Q, and η for Baseline PBCF and Modified PBCF with -5 Degree Installation Angle

Table 13: Effect of 2-Degree PBCF Modification on Propeller Performance

J	Experiment		Present Result (Baseline PBCF)		Present Result (Modified PBCF)	
	KT	KQ	KT	KQ	KT	KQ
0.346	0.3700	0.0750	0.3719	0.0599	0.3797	0.0594
0.415	0.3600	0.0710	0.3345	0.0555	0.3509	0.0558
0.518	0.3300	0.0630	0.2972	0.0502	0.3064	0.0501
0.592	0.2900	0.0560	0.2682	0.0462	0.2737	0.0459
0.691	0.2400	0.0480	0.2269	0.0406	0.2296	0.0403

ΔKT Exp. Vs. Baseline PBCF	ΔKQ Exp. Vs. Baseline PBCF	ΔKT Exp. Vs. Modified PBCF	ΔKQ Exp. Vs. Modified PBCF	ΔKT Baseline Vs. Modified PBCF	ΔKQ Baseline Vs. Modifed PBCF
0.5078	-20.1152	2.6214	-20.7538	2.1030	-0.7993
-7.0738	-21.8577	-2.5168	-21.4101	4.9039	0.5729
-9.9342	-20.3422	-7.1403	-20.5160	3.1020	-0.2182
-7.5256	-17.5764	-5.6046	-17.9516	2.0774	-0.4553
-5.4654	-15.5180	-4.3394	-16.0524	1.1912	-0.6325

η Exp.	η present result (Baseline PBCF)	η present result (Modified PBCF)	Δη% Exp. Vs. Baseline PBCF	Δη% Exp. Vs. Modified PBCF	Δη% Baseline. Vs. Modified PBCF
0.2716	0.3417	0.3517	25.8159	29.4969	2.9257
0.3348	0.3981	0.4152	18.9192	24.0404	4.3064
0.4317	0.4881	0.5043	13.0660	16.8282	3.3274
0.4877	0.5472	0.5611	12.1940	15.0485	2.5442
0.5497	0.6151	0.6264	11.8991	13.9528	1.8353

Figure 19 shows the velocity contours at J = 0.415 for (a) Baseline Propeller without PBCF and (b) Propeller with PBCF modification (model 2). As compared to baseline propeller, the PBCF modification results in more varying flow velocities. For example, at Z = -2.333 m on the central axis (0 mm), the baseline velocity is 7.107 m/s, while the modified version decreases to 4.140 m/s. In contrast, at positions 100 mm and 200 mm, especially closer to the propeller center (Z = -2.000 m), the modified version increases to 15.494 m/s from 13.610 m/s at the baseline. The PBCF modification results in better flow dynamics around the propeller. In addition, at Z = -1.67 m, the flow velocity increases from 7.74 m/s (baseline) to 8.25 m/s (modified), which indicates improving thrust efficiency. However, the PBCF modification also introduces significant turbulence and potential cavitation. It infers that further adjustment of the propeller design is needed to optimize the flow, reduce turbulence, and address the

cavitation issue for overall efficiency improvement as reported by (Li *et al.*, 2024). In addition, Figure 20 shows that the PBCF modification significantly improves the propeller efficiency compared to the baseline model. In the baseline model, the leading edge of the propeller experiences vortex and turbulence, increasing the fluid velocity (from 5 m/s to 12 m/s) and creating negative pressure (-76.528 Pa to -39.286 Pa). These results increased drag and decreased efficiency. In contrast, the PBCF modified model reduces vortex and turbulence which means directing the fluid flow more effectively. Although some areas of experience decreased in velocity (from 0.5 m/s to 8 m/s), the overall flow is more streamlined, with less negative pressure from vortex formation. This results in better propeller efficiency, reducing drag, and improving overall performance.

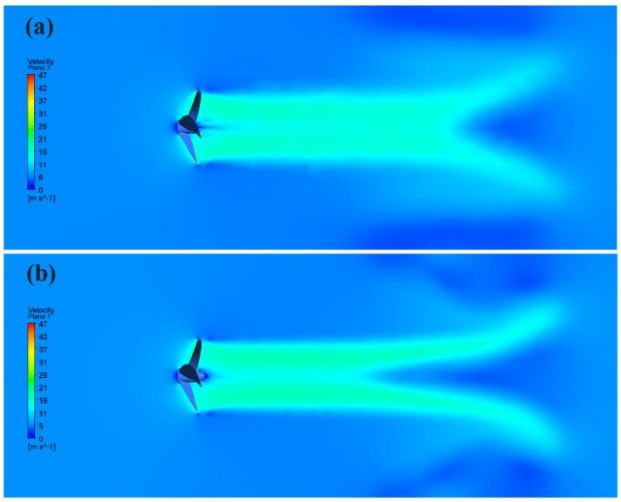

Fig.19: Velocity contour at J = 0.415 (a) Baseline Propeller without PBCF (b) Propeller with modification PBCF

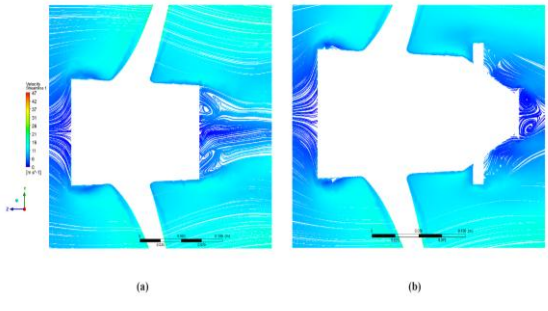

Fig. 20: Comparison of flow streamlines between (a) the baseline model and (b) the modified model with PBCF

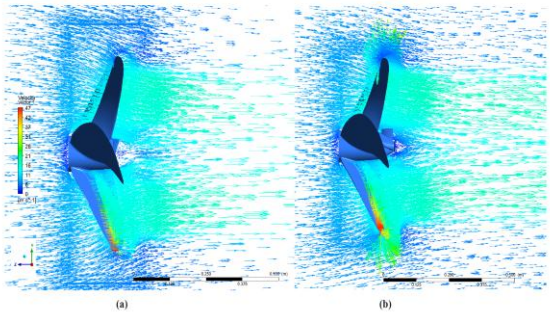

Fig. 21: Comparison of velocity vector between (a) the baseline model and (b) the modified model with PBCF

Figure 21 shows the vectors of water flow velocities affected by two propeller models: (a) the baseline model on the left and (b) the modified model with PBCF on the right. In the baseline model, the flow around the propeller is more turbulent, indicated by shorter and more irregular arrows which reflect high turbulence. In the contrary, the modified model with PBCF shows a smoother and more regular flow, with longer and straighter arrows, indicating less turbulence and more directional flow. The PBCF effectively directs the water flow, so it reduces eddies and turbulence around the propeller. It results in in smaller vortices and a more focused flow behind the propeller. The reduction in turbulence reduces energy losses and increases thrust, thereby improve the overall propeller efficiency.

Figure 22 shows the lines of water flow from the propeller at a specific time (j=0.415). It compares the flow patterns with and without PBCF. The front view informs the baseline model without PBCF (a) shows more chaotic and less uniform flow lines, indicating higher turbulence. In contrast, the model with PBCF (b) displays more

regular and uniform flow lines, inferring a smoother and more organized flow pattern. While Figure 23 showing the back view indicates the baseline propeller (a) produces somewhat regular flow lines, although some areas of turbulence are still visible. However, the model with PBCF (b) shows much more organized and uniform flow lines, reflecting a more controlled and smoother flow. Overall, it can be concluded that the modification with PBCF significantly improves the flow pattern around the propeller, reducing turbulence and increasing flow efficiency, as shown in Figure 24.

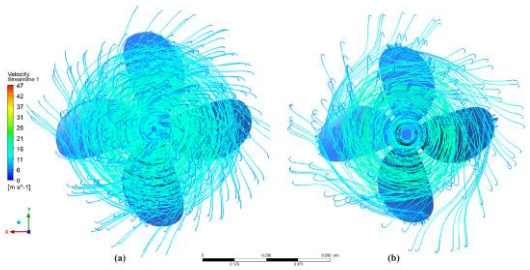

Fig. 22: Streamline velocity contour at J = 0.415 (a) Baseline Propeller without PBCF and (b) Propeller with modification PBCF (model 2) front view

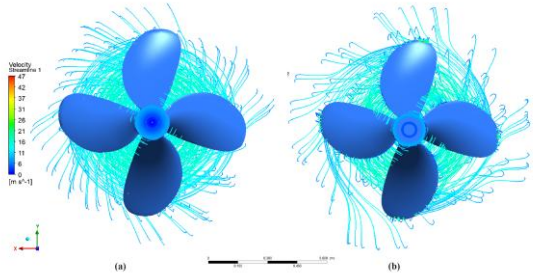

Fig. 23: Streamline velocity contour at J = 0.415 (a) Baseline Propeller without PBCF and (b) Propeller with modification PBCF (model 2) back view

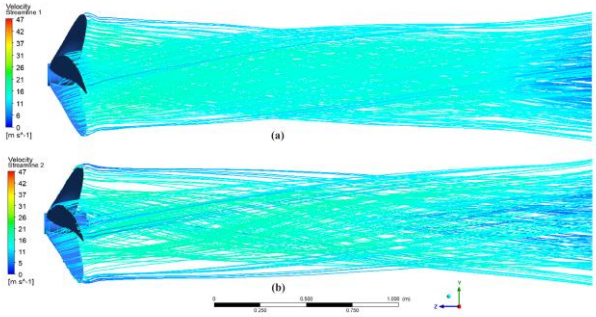

Fig. 24: Streamline velocity contour at J = 0.415 (a) Baseline Propeller without PBCF and (b) Propeller with modification PBCF (model 2) side view

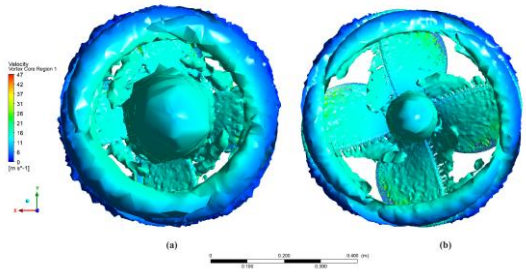

Fig. 25: Vortex velocity contour at J = 0.415 (a) Baseline Propeller without PBCF and (b) Propeller with modification PBCF (model 2) front view

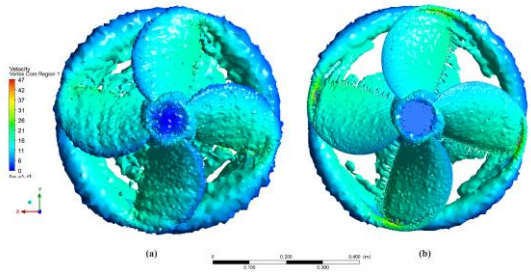

Fig. 26: Vortex velocity contour at J = 0.415 (a) **Baseline** Propeller without PBCF and (b) Propeller with modification PBCF (model 2) back view

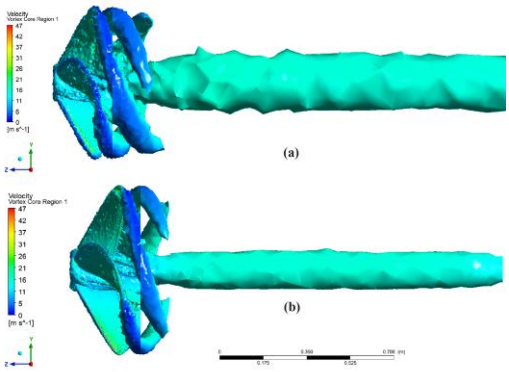

Fig. 27: Vortex velocity contour at J = 0.415 (a) Baseline Propeller without PBCF (b) Propeller with modification PBCF (model 2)

Figure 25 shows the front view comparison between the vortex velocity contours of two propeller configurations: (a) baseline without PBCF and (b) propeller with PBCF modification (model 2). The baseline propeller shows a more chaotic and irregular vortex pattern, while the propeller with PBCF modification displays a more structured and smooth vortex flow. This result indicates that PBCF modification potentially improves efficiency. The back view shown in Figure 26 further highlights this difference; the baseline propeller shows a more scattered and uneven vortex structure, while the propeller modified with PBCF shows a more coherent and controlled vortex flow. These results indicate that the PBCF modification significantly improves the vortex behavior of the propeller. It results in a more organized and streamlined flow pattern, as shown in Figure 27.

The pressure contours at J = 0.415 for (a) the baseline propeller without PBCF and (b) the propeller with PBCF can be seen in Figure 28. Figure 28 indicates that the PBCF modification generally decreases the pressure around the propeller. For example, at Z = -1,000 m, the baseline pressure is -26,413.30 Pa, while with PBCF it decreases to -46,052.98 Pa. It is due to more even pressure distribution and reduced drag. Figure 30 strengthens the claim that the optimized PBCF significantly reduce the low-pressure zone and drag by addressing the vortex pressure at the hub, leading to improved efficiency. The baseline model shows negative pressures between -300,000 and -174,242 Pa, while the modified model shows lower pressures and faster flow velocities, indicating a reduction in the excessive low-pressure area. Figure 31 shows that at the leading surface of the propeller, the pressure increases due to flow deceleration, with the modified model showing higher pressures and improved lift compared to the baseline. Around the hub, PBCFs help to manage the flow more effectively, reduce negative pressure and increase overall efficiency.

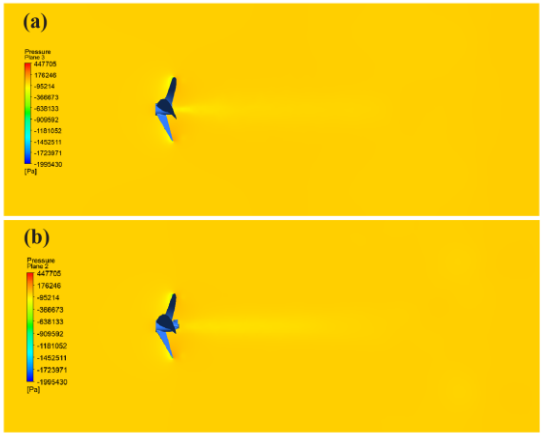

Fig. 28: Pressure contour at J = 0.415 (a) Baseline Propeller without PBCF (b) Propeller with modification PBCF

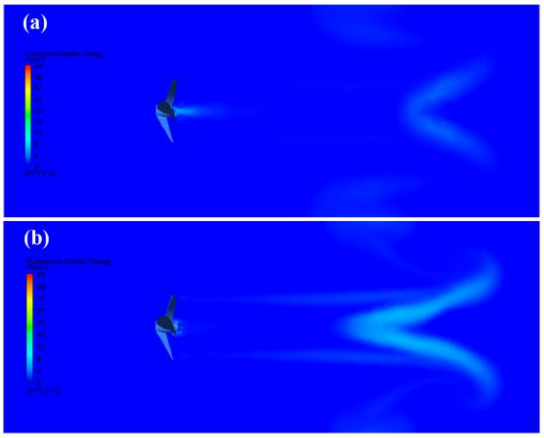

Fig. 29: TKE contour at J = 0.415 (a) Baseline Propeller without PBCF (b) Propeller with modification PBCF

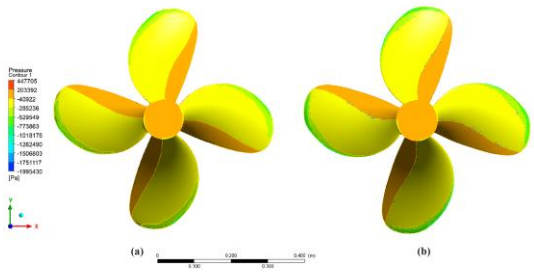

Fig. 30: Pressure distribution on the surface of the propeller (a) baseline and (b) modification model 2 back view

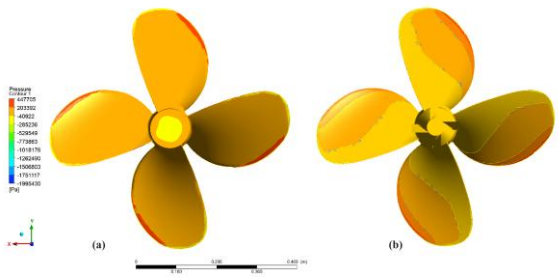

Fig. 31: Pressure distribution on the surface of the propeller (a) baseline and (b) modification model 2 front view

Figure 29 shows the Turbulence Kinetic Energy (TKE) contours for the propeller with and without PBCF. At Z = -1.67 m, the TKE of baseline propeller and propeller with PBCF is 2.24 m²/s², and 1.05 m²/s², respectively. The TKE significant reduction of propeller with PBCFs indicates less turbulence around the propeller, contributing to reduced drag and increased thrust efficiency. Although the TKE of propeller with PBCF is slightly higher at j = 0.415 due to flow adjustment, overall, PBCF produce more regulated flow behind the propeller. As result, PBCF increases overall flow efficiency, in spite of postering local turbulence.

4. Conclusions

This study conducted a CFD-based performance evaluation of the Wageningen B-series propeller equipped with modified PBCF. Among the tested configurations, a 2° installation angle applied to NACA 4412-based PBCF achieved the highest hydrodynamic efficiency. Although a slight reduction in K_T and K_Q was observed—approximately 2.1% and 1.7%, respectively, compared to the baseline—the overall propeller efficiency increased by up to 4% relative to the unmodified CFD model, and by 24.3% when compared with experimental data at an advance ratio of J = 0.415.

This efficiency gain is primarily attributed to improved flow uniformity and reduced hub vortex strength, resulting in lower drag and better wake alignment. Additionally, the optimized PBCF configuration mitigated negative pressure regions commonly associated with cavitation, thus contributing not only to energy savings but also to reduced cavitation-induced erosion risk. These outcomes underscore the value of fine-tuning PBCF geometry, especially for medium-speed, high-load vessels such as Ro-Ro ferries or coastal cargo ships utilizing similar propeller types (e.g., B4-70, Ka-series).

This research advances marine propulsion optimization by introducing a divergent-type boss cap design combined with NACA 4412 profiles, tested across installation angle variations of ±5° relative to the local rake angle (ε). Unlike earlier studies focusing on convergent boss caps or fixed fin designs, this study emphasizes angle-sensitive performance tuning, offering deeper insight into the interaction between PBCF geometry and flow behavior.

The CFD results were partially validated against experimental data. While the simulations captured consistent performance trends, discrepancies in thrust and torque—up to 5%—were noted. These are likely due to idealized boundary conditions and the absence of full-scale Reynolds number effects. This highlights the need for further validation through scaled model testing or towing tank experiments, especially to refine turbulence modeling near tip vortices and boundary layers.

For future research, we recommend integrating advanced shape optimization methods—such as genetic algorithms and gradient-based techniques—to refine airfoil geometry, thickness, and tip chord distribution. Multivariable analyses can support this effort. Incorporating Fluid-Structure Interaction (FSI) into CFD simulations would also enhance realism, especially for flexible or composite PBCF materials under dynamic loading.

Experimental validation remains essential. Controlled testing in cavitation tunnels or towing tanks should include pressure mapping, flow visualization, and cavitation pattern analysis. Future studies should also address cavitation and acoustic behavior, evaluating parameters like cavitation inception index (σi), bubble collapse dynamics, and noise emissions using models such as Schnerr-Sauer or Zwart-Gerber-Belamri.

Finally, practical implementation considerations—including manufacturability, material selection, and retrofitting feasibility—must be assessed. A comprehensive cost-benefit and lifecycle analysis is recommended to evaluate trade-offs between added resistance, initial investment, and long-term fuel savings, thereby supporting the viability of PBCF integration in full-scale marine applications.

Acknowledgements

The authors gratefully acknowledge the financial support provided by Gunadarma University

References

Adietya, B. A., Syahab, H., Indiaryanto, M., Aryawan, W. D., and Utama, I. K. A. P. (2024): Influence evaluation of open propellers with boss cap fins: case studies on types b4-70 and ka4-70. CFD Letters, 16(9). https://doi.org/10.37934/cfdl.16.9.143177

Adietya, B. A., Utama, I. K. A. P., Aryawan, W. D., Nasir, M., Nurcholis, Indiaryanto, M., Asrowibowo, N., Permana, R. D., and Nurhadi. (2023): Numerical and experimental investigations into the characteristics of wageningen b4-70 series of propeller with boss cap fins. CFD Letters, 15(10). https://doi.org/10.37934/cfdl.15.10.152169

Barnitsas, M. M., Ray, D., and Kinley, P. (1981): KT, KQ and efficiency curves for the Wageningen B-series propellers. University of Michigan.

Chandukrishna, Y., and Venkatesh, T. N. (2023): Numerical investigation of aerodynamically efficient wing tip-mounted propeller configuration using coupled RANS–BEM approach. Aircraft Engineering and Aerospace Technology, 95(6), 995–1001. https://doi.org/10.1108/AEAT-09-2022-0254

Fitriadhy, A., Adam, N. A., and Bakar, A. A. (2023): Computational investigation into the effect of pitch ratio on b-series propeller performance. Journal of Naval Architecture and Marine Engineering, 20(2). https://doi.org/10.3329/jname.v20i2.67965

Gavidia, J. C. R, Furlan Chinelatto, G., Basso, M., da Ponte Souza, J. P., Soltanmohammadi, R., Campane Vidal, A., Goldstein, R. H., and Mohammadizadeh, S. (2023): Utilizing integrated artificial intelligence for characterizing mineralogy and facies in a pre-salt carbonate reservoir, Santos Basin, Brazil, using cores, wireline logs, and multi-mineral petrophysical evaluation. Geoenergy Science and Engineering, 231, 212303. https://doi.org/10.1016/j.geoen.2023.212303

Gavidia, J. C. R., Mohammadizadeh, S., Chinelatto, G. F., Basso, M., da Ponte Souza, J. P., Portillo, L. E. D., Eltom, H. A., Vidal, A. C., and Goldstein, R. H. (2024): Bridging the gap: Integrating static and dynamic data for improved permeability modeling and super k zone detection in vuggy reservoirs. Geoenergy Science and Engineering, 241, 213152. https://doi.org/10.1016/j.geoen.2024.213152

Göksu, B., Bayraktar, M., and Yüksel, O. (2024): The evaluation of propeller boss cap fins effects for different pitches and positions in open water conditions. Journal of Ship Production and Design, 40(02), 102–111. https://doi.org/10.5957/JSPD.08230017

Hasan, S. M. R., and Karim, M. M. (2023): Energy-efficient inland cargo ship design based on fuel consumption and CO2 emission control using CFD. Journal of Naval Architecture and Marine Engineering, 20(3). https://doi.org/10.3329/jname.v20i3.63664

Hunt, J. C. R. (1973): Mathematical Models of Turbulence. By B. E. LAUNDER and D. B. SPALDING. Academic Press, 1972. 169 pp. £2.50 or $7.50. Journal of Fluid Mechanics, 57(4), 826–828. https://doi.org/10.1017/S0022112073222048

Ismail, K., Patah, N. E. F. A., Mohtar, M., Kamal, I. Z. M., Mohamed, E. A. A. E., and Ahmed, Y. A. (2024): Investigation on the Interaction of Controllable Pitch Propeller with Boss Cap Fins at Slow-Ahead, Half-Ahead, and Full-Ahead Position. In A. Ismail, F. N. Zulkipli, M. A. Mohd Daril, and A. Öchsner (Eds.), Engineering Frontiers: A Multidisciplinary Odyssey (pp. 299–319). Springer Nature Switzerland. https://doi.org/10.1007/978-3-031-56844-2_27

Kim, D.-H., Park, J.-C., Jeon, G.-M., and Shin, M.-S. (2021): CFD simulation for estimating efficiency of pbcf installed on a 176k bulk carrier under both pow and self-propulsion conditions. Processes, 9(7). https://doi.org/10.3390/pr9071192

Launder, B. E. (1995): Turbulence Modelling for CFD. By D. C. WILCOX. DCW Industries Inc., 1993. 460pp. $75. Journal of Fluid Mechanics, 289, 406–407. https://doi.org/10.1017/S0022112095211388

Lee, M., Park, G., Park, C., and Kim, C. (2020): Improvement of grid independence test for computational fluid dynamics model of building based on grid resolution. Advances in Civil Engineering, 2020, e8827936. https://doi.org/10.1155/2020/8827936

Lee, M.-H., Kim, C.-M., Park, G.-Y., Choi, C.-H., and Park, C.-Y. (2020): Grid independence test of computational fluid dynamics model for indoor airflow analysis. Journal of Korean Institute of Architectural Sustainable Environment and Building Systems, 14(2), 183–194. https://doi.org/10.22696/jkiaebs.20200017

Lee, S.-S. (2024). Analysis of the effects of EEDI and EEXI implementation on CO2 emissions reduction in ships. Ocean Engineering, 295, 116877. https://doi.org/10.1016/j.oceaneng.2024.116877

Li, C., Cao, Y., Xu, H., Jiang, T., and Liu, C. (2024): Energy-saving optimization design of propeller boss cap fin based on BP neural network coupled with Northern Goshawk optimization algorithm. International Journal of Energy Research, 2024(1), 8424160. https://doi.org/10.1155/2024/8424160

Lovibond, O., Elbarghthi, A. F. A., Dvorak, V., and Wen, C. (2023): Numerical analysis of propellers for electric boats using computational fluid dynamics modelling. Energy Conversion and Management: X, 17, 100349. https://doi.org/10.1016/j.ecmx.2023.100349

Martinelli, M., Villa, D., and Gaggero, S. (2021): Design and application of propeller boss cap fins to ducted propellers. In Maritime Technology and Engineering 5 Volume 1. CRC Press.

Mohammadizadeh, S., Dalfré Filho, J. G., Sampaio Descovi, C., Genovez, A. I. B., and Teixeira Buttignol, T. E. (2024): Experimental analysis of cavitation erosion: Parameter sensitivity and testing protocols. Coatings, 14(10). https://doi.org/10.3390/coatings14101288

Mohammadizadeh, S., Moghaddam, M. A., and Talebbeydokhti, N. (2021): Analysis of flow in porous media using combined pressurized-free surface network. Journal of Porous Media, 24(10). https://doi.org/10.1615/JPorMedia.2021025407

Pantel, H., Falissard, F., and Dufour, G. (2024): Assessment of Reynolds-Averaged Navier–Stokes/Blade element theory body force method for propeller modeling. AIAA Journal, 62(2), 758–775. https://doi.org/10.2514/1.J063302

Rastogi, A., and Mathew, M. (2022): Cavitation visualization and prediction of propeller characteristics of INSEAN E779A propeller using sliding mesh model. OCEANS 2022 - Chennai, 1–8. https://doi.org/10.1109/OCEANSChennai45887.2022.9775459

Tarafder, M. S., Haque, M. I., Asaduzzaman, M., and Laku, M. Z. I. (2023): Numerical investigation of hydrodynamic performance of conventional and ducted propellers. Journal of Naval Architecture and Marine Engineering, 20(3). https://doi.org/10.3329/jname.v20i3.69990

Vásconez Garcia, R. G., Mohammadizadeh, S., Avansi, M. C. K., Basilici, G., Bomfim, L. da S., Cunha, O. R., Soares, M. V. T., Mesquita, Á. F., Mahjour, S. K., and Vidal, A. C. (2024): Geological insights from porosity analysis for sustainable development of Santos Basin's presalt carbonate reservoir. Sustainability, 16(13). https://doi.org/10.3390/su16135730

Wang, Y., Xiao, Y., Fang, B., Li, W., Duan, C., Zhang, W., and Hu, J. (2025): Effect of blade number on tip vortex cavitation of propeller. Journal of Marine Science and Engineering, 13(5). https://doi.org/10.3390/jmse13050915

Yin, C., Rosenvinge, C. K., Sandland, M. P., Ehlers, A., and Shin, K. W. (2023): Improve ship propeller efficiency via optimum design of propeller boss cap fins. Energies, 16(3). https://doi.org/10.3390/en16031247

Zhang, L., Hou, L., and Tao, Y. (2023). Analysis on performances and flow fields of a single waterjet propeller based on SST k −ω model. Journal of Nanoelectronics and Optoelectronics, 18(9), 1021–1036. https://doi.org/10.1166/jno.2023.3477

Zhang, Y.-X., Zhu, Y.-X., Zhang, L., Yang, Z.-T., and Li, Y.-L. (2025): CFD study of propeller tip vortex cavitation. International Journal of Multiphase Flow, 182, 105020. https://doi.org/10.1016/j.ijmultiphaseflow.2024.105020